



Article

Comparison of Three Approaches for Estimating Understory Biomass in Yanshan Mountains

Yuanqi Li ^{1,2}, Ronghai Hu ^{1,2} , Yuzhen Xing ², Zhe Pang ² , Zhi Chen ^{1,2,3} and Haishan Niu ^{1,2,*}

¹ Beijing Yanshan Earth Critical Zone National Research Station, University of Chinese Academy of Sciences, Beijing 101408, China; liyuanqi21@mailsucas.ac.cn (Y.L.); huronghai@ucas.ac.cn (R.H.); chenz@igsnr.ac.cn (Z.C.)

² College of Resources and Environment, University of Chinese Academy of Sciences, Beijing 100049, China; xingyuzhen20@mailsucas.ac.cn (Y.X.); pangzhe@ucas.ac.cn (Z.P.)

³ Key Laboratory of Ecosystem Network Observation and Modeling, Institute of Geographic Sciences and Natural Resources Research, Chinese Academy of Sciences, Beijing 100101, China

* Correspondence: niuhs@ucas.ac.cn

Abstract: Aboveground biomass (AGB) of shrubs and low-statured trees constitutes a substantial portion of the total carbon pool in temperate forest ecosystems, contributing much to local biodiversity, altering tree-regeneration growth rates, and determining above- and belowground food webs. Accurate quantification of AGB at the shrub layer is crucial for ecological modeling and still remains a challenge. Several methods for estimating understory biomass, including inventory and remote sensing-based methods, need to be evaluated against measured datasets. In this study, we acquired 158 individual terrestrial laser scans (TLS) across 45 sites in the Yanshan Mountains and generated metrics including leaf area and stem volume from TLS data using voxel- and non-voxel-based approaches in both leaf-on and leaf-off scenarios. Allometric equations were applied using field-measured parameters as an inventory approach. The results indicated that allometric equations using crown area and height yielded results with higher accuracy than other inventory approach parameters (R^2 and RMSE ranging from 0.47 to 0.91 and 12.38 to 38.11 g, respectively). The voxel-based approach using TLS data provided results with R^2 and RMSE ranging from 0.86 to 0.96 and 6.43 to 21.03 g. Additionally, the non-voxel-based approach provided similar or slightly better results compared to the voxel-based approach (R^2 and RMSE ranging from 0.93 to 0.96 and 4.23 to 11.27 g, respectively) while avoiding the complexity of selecting the optimal voxel size that arises during voxelization.

Keywords: understory AGB estimation; TLS; voxel size; non-voxel-based approach



Citation: Li, Y.; Hu, R.; Xing, Y.; Pang, Z.; Chen, Z.; Niu, H. Comparison of Three Approaches for Estimating Understory Biomass in Yanshan Mountains. *Remote Sens.* **2024**, *16*, 1060. <https://doi.org/10.3390/rs16061060>

Academic Editor: John F. Weishampel

Received: 17 January 2024

Revised: 6 March 2024

Accepted: 15 March 2024

Published: 16 March 2024



Copyright: © 2024 by the authors. Licensee MDPI, Basel, Switzerland. This article is an open access article distributed under the terms and conditions of the Creative Commons Attribution (CC BY) license (<https://creativecommons.org/licenses/by/4.0/>).

1. Introduction

Aboveground biomass (AGB), an important element in forest management and policymaking [1], is defined as the total dry mass allocated to the live and dead tissues and organs of aboveground vegetation structures [2,3]. About 80% of the total aboveground biomass of the terrestrial ecosystem is stored within forests [4,5]. Therefore, accurate forest biomass estimation is essential for monitoring and understanding how terrestrial ecosystems function and change in response to climate change [6,7]. Understory vegetation plays an integral role in forests, significantly affecting gross primary productivity, respiration, and carbon and nutrient fluxes [8–10], and it is considered to be an overall indicator of forest health [11,12].

Understory biomass estimation at a fine spatial resolution over large difficult-to-access areas like mountain terrain remains a challenge when conducted through field measurements [13]. The AGB of understory vegetation is most accurately measured with destructive sampling. However, such inventory methods can be labor-intensive and time-consuming. Thus, it is often used to obtain the AGB for a small amount of representative

vegetation for developing allometric equations using nonlinear or linear transformation of field-measured parameters, including diameter, height, canopy cover, etc. [14]. However, the widely used allometric equations mainly relate to forest trees or large shrub biomass predictions [15,16], which could undermine the estimation accuracy when applied to low-stature trees and shrubs. Although field measurements provide reliable calibration data for predictions [17], the applicability of allometric equations would still be affected due to the limited sample size and range when applied at an extensive scale in forest ecosystems [18,19]. Hence, there is a need to evaluate more efficient and nondestructive approaches for predicting and mapping understory biomass at individual scale to better facilitate the quantification of understory biomass.

As an active remote sensing approach, LiDAR (Light Detection and Ranging) allows accurate measurement of distances by transmitting laser pulses and analyzing the returned energy as a function of time [20], and it has emerged as a feasible tool for extracting crucial forest structure parameters [21]. Over the past two decades, LiDAR developed rapidly with multiple platforms, including satellite platforms (ICESat and GEDI, and spaceborne laser scanning, SLS), airborne platforms including manned aircraft and drones (airborne laser scanning, ALS), and ground platforms (terrestrial laser scanning, TLS), providing technical support for monitoring a wide range of forest dynamics changes [22]. Airborne laser scanning (ALS) is well-established in forestry research for characterizing three-dimensional variation in a tree canopy structure at plot or stand level [23] and has proven to be a highly accurate tool for assessing tree volume [24] and biomass [25] in forested stands. However, scanning of the understory can be problematic, underestimating height and volume up to 30–50% [26,27] due to the low point density of ALS, typically less than 10 pts m⁻², relative to shrub size [28].

In comparison to ALS, terrestrial laser scanning (TLS) can collect a much higher point cloud density (1000 pts/m²), greatly improving the measurement accuracy of vegetation structure. Although the scanning range is limited, it is suitable for collecting 3D structures at a fine scale and minimizing canopy occlusion in contrast with ALS [15], enabling the possibility of quantifying volume or biomass [21,29,30] and calculating leaf indices, including the leaf area index (LAI) and leaf area density (LAD) [31–33]. The voxel-based approach has proven to be effective in quantifying structural parameters and estimating the biomass of trees and surface fuelbeds using TLS data [34–36]. The specification of voxel size in the process of voxelization has proven to have a significant impact on the estimation accuracy in previous studies, and optimal voxel size needs to be determined [37,38]. Among vegetation complexity, subcanopy structure, and clumping effect, several factors are proposed to be influencing the value of optimal voxel size [39,40], and measures have been taken to tackle this problem, including limiting occlusion by conducting multiple scans and introducing correction factors in different voxel sizes [41], yet the specification of optimal voxel size still remains contradictory in different studies [42–44]. Here, we applied a non-voxel-based approach as an alternative and conducted comparisons to evaluate its performance for understory biomass estimation.

According to a previous field survey, the morphology of low-statured trees in the Yanshan Mountains was similar to that of the tree species. Thus, inventory-based parameters like diameter, height, and crown area can be effective in describing their structure; the AGB of the low-statured trees can be more accurately estimated using the inventory method, whereas shrub species, owing to their irregular morphology and inventory parameters like basal diameter and height, are difficult to acquire and may not be effective in describing structural information at individual scale, thus affecting accuracy in biomass estimation [45]. Therefore, evaluating other approaches and determining a better solution for understory quantification in the Yanshan Mountains are necessary. To achieve this goal, the objective of this study is broken down into the following more specific objectives: (1) to test the feasibility of field-measured parameters in estimating understory aboveground biomass; (2) to evaluate the efficiency of using TLS metrics as predictors in biomass models at individual scale through the voxel-based approach and evaluate the impact of voxel size

on estimation results; and (3) to apply a non-voxel-based approach for comparison and bypass the impact of the selection of voxel sizes in the voxelization process.

2. Materials and Methods

2.1. Study Area

The study area was the Beijing Yanshan Earth Critical Zone National Research Station located in the University of Chinese Academy of Science, Beijing ($116^{\circ}39'E$, $40^{\circ}25'N$), with an elevation of approximately 50–100 m and a slope ranging from 0° to 45° , covering a total area of approximately 250 ha (Figure 1). Vegetation types in this area are temperate mixed broadleaf–conifer forest at plains and low-altitude mountain areas and shrubs at mid- to high-altitude mountain areas. Dominated species include Chinese Pine (*Pinus tabuliformis*), Date Plum (*Diospyros lotus*), and Mongolian Oak (*Quercus mongolica*) for trees, and Spine Jujube (*Ziziphus jujuba*), *Vitex negundo*, and small-flower Grewia (*Grewia biloba*) for shrubs.

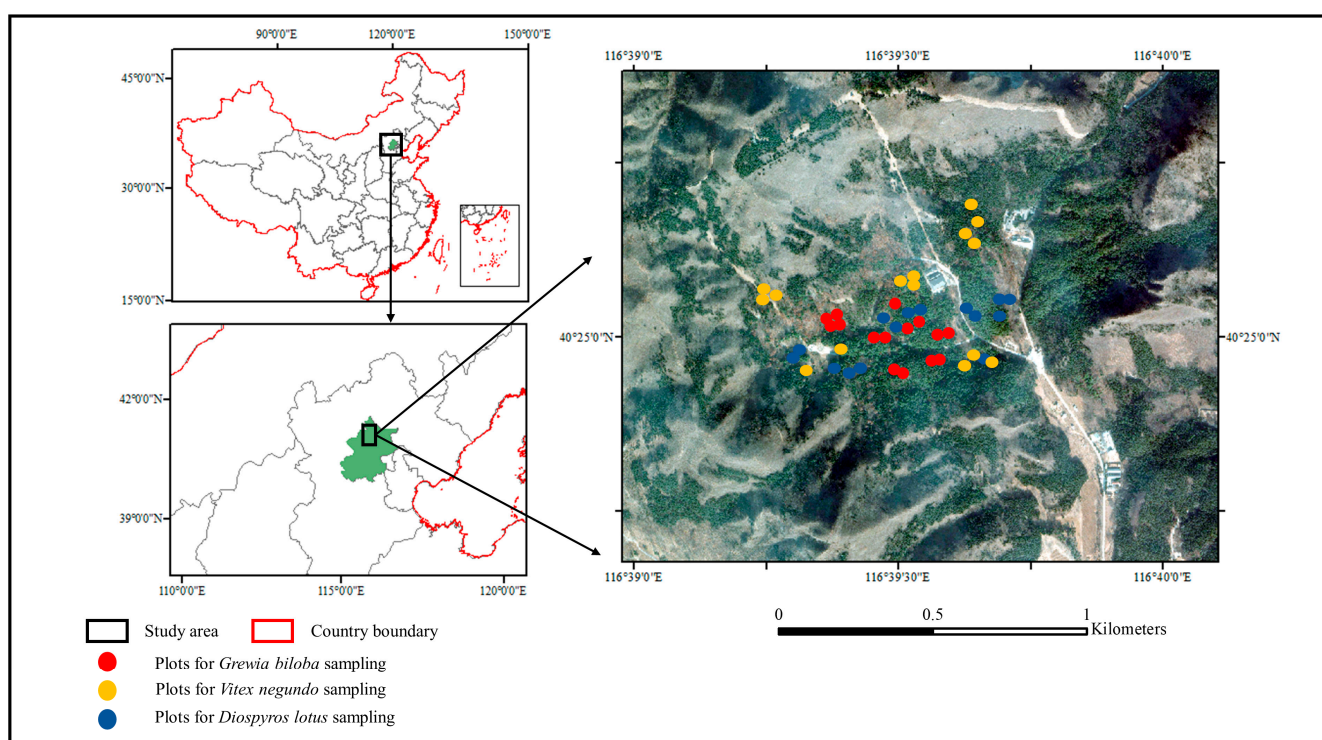


Figure 1. Study area with spatial distribution of understory vegetation plots.

2.2. TLS and Field Data Acquisition

We conducted our study targeting three common understory species, including two dominant shrub species, namely *Grewia biloba* and *Vitex negundo*, and one low-statured tree species, *Diospyros lotus*. To evaluate the accuracy and universality of the three AGB estimation approaches at shrub level, plants in both regular and irregular morphology were selected in both broadleaf and coniferous forests, and forty-five sampling plots were established, with fifteen each for the three studied species. Field research was conducted following the procedure shown in (Figure 2a) during growing seasons in 2023. All inventory data, including basal diameter, height, crown area, crown length, and crown width, were measured using diameter tape, and scanning was performed with a Trimble X7 terrestrial laser scanner (Trimble Inc., Westminster, CO, USA) (Table 1). The point cloud data (PCD) for each station were exported to PTX format, containing the scanner location and information (coordinates and intensity) of all emitted laser pulses regardless of whether the pulses obtained a return.

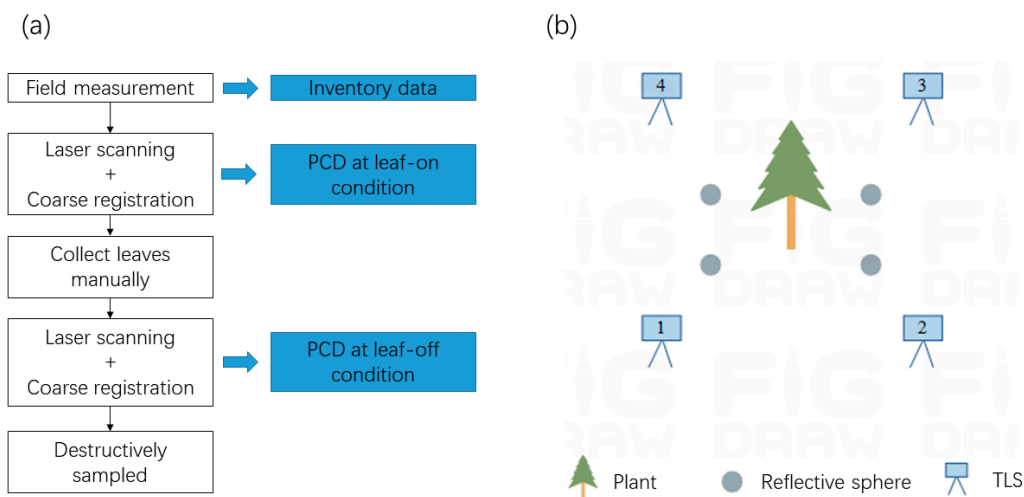


Figure 2. Illustration of (a) TLS and ground data acquisition workflow and (b) arrangements of the sampled quadrats.

Table 1. Trimble X7 technical specifications.

Attribute	Specification
Wavelength	1550 nm, invisible
Field of View	360° (horizontal) × 282° (vertical)
Scanning Frequency	>500 kHz
Range	0.6 m–80 m
Range Accuracy	2 mm
Angular Accuracy	21"
3D Point Accuracy	2.4 mm at 10 m, 3.5 mm at 20 m, 6.0 mm at 40 m

Due to occlusion and the difficult mountain terrains, we were required to shift the laser scanner to various positions to ensure high point density (the point density is determined by the set angular resolution and the distance between the scanned object and TLS sensor) and the full coverage of data in each plot, which generally resulted in 2–4 stations of scanning at opposite angles (Figure 2b). Coarse registration of PCD was performed using reflective spheres and three sets of paired points selected by visual interpolation from two corresponding stations using Trimble X7 software packages, which calculate the rotation matrix and translation vector and register point clouds of multiple scans into a local coordinate system with the center of the instrument at station one given a coordinate of (0, 0, 0). All leaf samples collected were first scanned using an EPSON scanner, and the leaf area (LA) was calculated using its package software. Then, both leaf and stem samples were oven-dried at 65 °C for 48 h or until a constant dry weight was reached. Separate dry weights of green and woody biomass were recorded for biomass regression for each sampled plant.

2.3. TLS Data Preprocessing

In the measurement of forest ecosystems, understory measurement accuracy is not stable due to scanning distance and occlusion of vegetation [29]; therefore, PCD preprocessing is required before further analysis, which consists of denoising, segmentation, classification, and registration (both coarse and refined). We applied the iterative closest point (ICP) algorithm as a refined registration approach in MATLAB (R2022a) to further improve the registration accuracy. In general, the ICP algorithm iterates over two steps: (1) find the corresponding set $k = [(p,q)]$ from the target point cloud p , and the source point cloud q transformed with the current transformation matrix T , which includes a 3×3 rotation matrix and a 1×3 translation vector. (2) Update the transformation T by minimizing an

objective function defined over the correspondence set K [46]. In this study, we applied RMSE as an indicator of registration accuracy (Figure 3a).

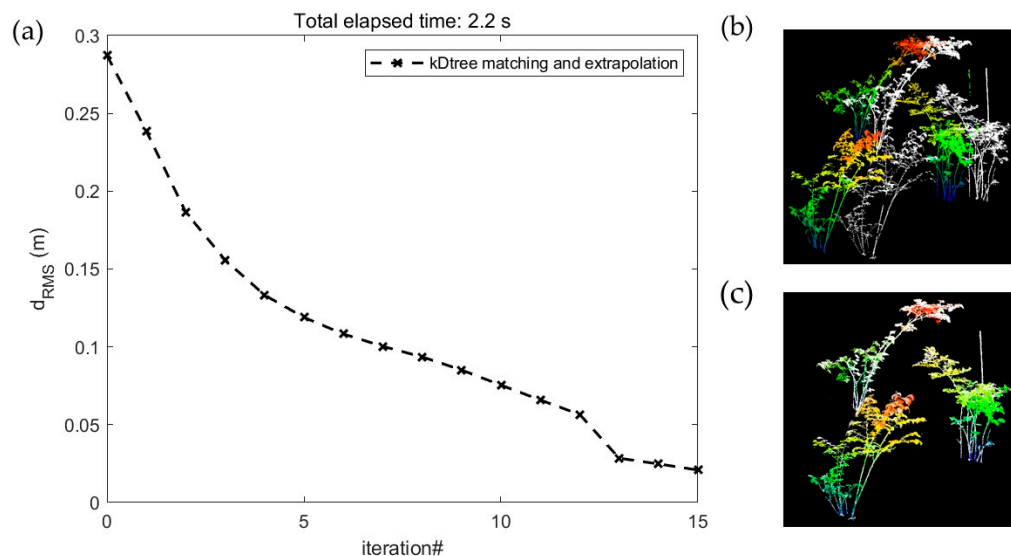


Figure 3. Illustration of refined registration using the point-to-point ICP algorithm: (a) registration accuracy in 15 iterations, and (b) visualization of the target point cloud (colored) and source point cloud (white) before refined registration and (c) after registration.

A statistical outlier removal (SOR) filter was applied to remove most points classified as noise (more information on the SOR filter can be found in Supplementary Materials). Each of the forty-five resulting PCD were then segmented to a radius of 3 m to 5 m depending on the vegetation's growth morphology and generally larger than the field quadrats to avoid clipping out stems that originated within the quadrats but extended outside of them. A cloth simulation filter (CSF) was applied to generate ground points, and the PCD of the studied plant were extracted using segmentation and a height threshold of 1 cm above ground. All denoising, segmentation, and classification were conducted in CloudCompare v2.12.4.

2.4. Volume and LA Calculation

2.4.1. Method Overview

The volume and LA derived from PCD were used as a proxy for the biomass of individual plants. To contrast the estimation results using the inventory approach, we formulated two schemes utilizing PCD: (a) estimating plant biomass with plant volume (aggregated model) and (b) estimating leaf and stem biomass separately (separated model) using calculated LA and stem volume from PCD, respectively (Figure 4). Three volume models, including voxel (voxel counting), convex hull (CH), and alpha shape (AS), were utilized and evaluated with measured biomass, while two LA calculation approaches, namely the voxel-based method and path length distribution method, were applied and evaluated in the process of estimating leaf biomass.

2.4.2. Volume Calculation with TLS Data

Three volume calculation methods were applied using PCD (Figure 5a) collected at both leaf-on and leaf-off conditions. The voxel-based approach (Figure 5b) divides 3D spaces into voxels (i.e., cubic volumes) of a given size (i.e., voxel size), which either contain laser returns (1) or are empty (0). Such a method allows voxels to represent multiple canopy levels (Z values) at the same X and Y coordinates. Volume can be calculated by multiplying the number of voxels classified as (1) and the given singular voxel volume. In recent studies, the voxel counting method has been applied successfully with TLS data on deriving biomass, LAI estimation, and fuelbed characterization [47,48]. However, a

lack of laser returns of the interior structure of the targeted plant due to occlusion from densely canopied vegetation may occur, leading to empty voxels and canopy voids, thus underestimating plant volume and causing errors in biomass estimation.

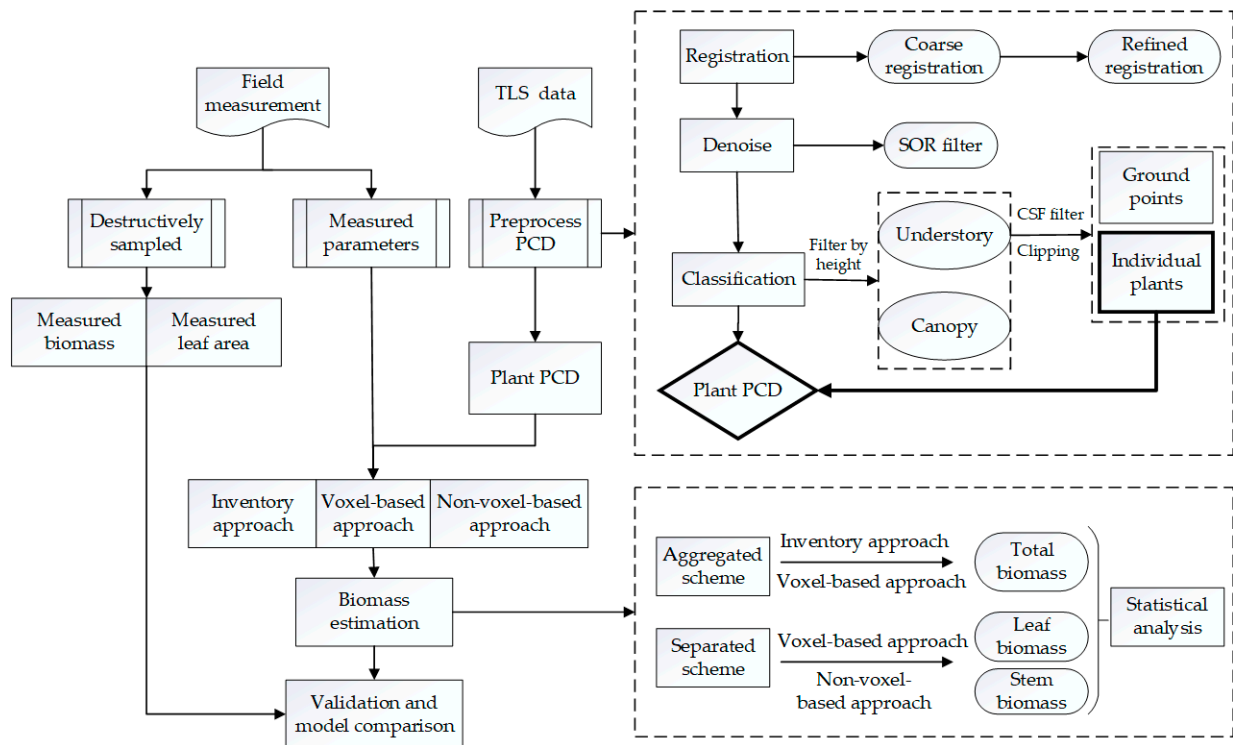


Figure 4. Data processing workflow.

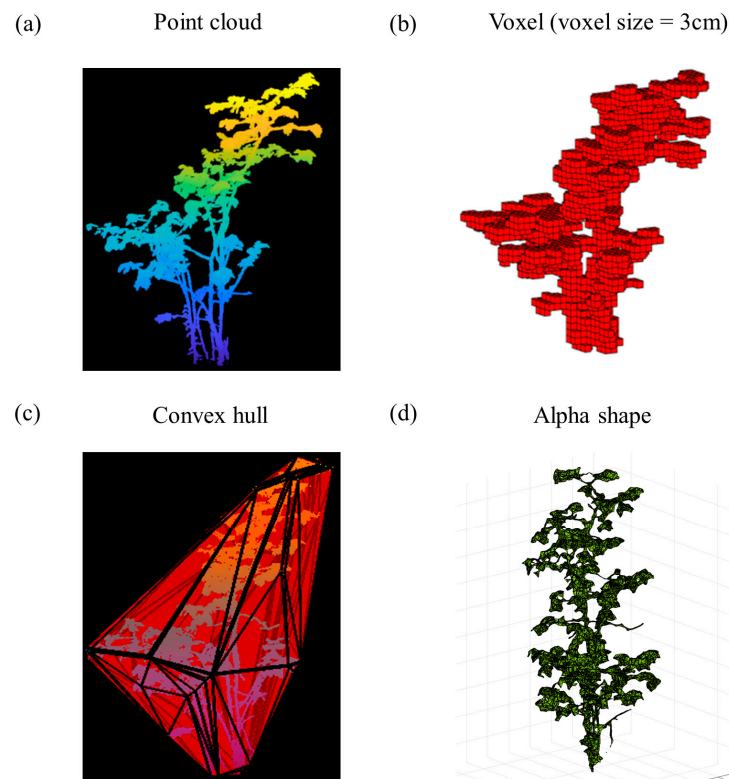


Figure 5. Illustration of the original point cloud (a) and three different volume estimation models derived from TLS, namely (b) voxel, (c) convex hull, and (d) alpha shape.

CH (Figure 5c) was applied to PCD as an alternative to the voxel counting approach. A convex hull is defined by an outer set of facets, embodying the entire point cloud and filling in the inner gaps. The CH processing in our study was conducted in MATLAB using the Quickhull algorithm. In contrast with the voxel model, CH overestimates the true volume of the targeted plant as the inner gaps are ignored, which can be excluded from the occlusion effect. Although both approaches can be applied with accurate results, the appropriateness of both methods depends on the density of the targeted vegetation; for instance, the voxel-based approach performs better when very limited parts of the vegetation are occluded, while CH can be more suitable for occasions when scanning a plant with complex and dense structure.

AS (Figure 5d) is a concave hull algorithm in which the simplex of the underlying triangulation is compared with the specific α , deleting the simplex with an empty external sphere and a square radius greater than the α . Then, the volume of the 3D object is calculated. It should be noted that, when α is large enough, the 3D structure will be similar to that of the CH [49]. In this study, we set the parameter α to a constant of 0.05 to exclude smaller pores within the canopy and contain as much detailed structural information as possible without creating discontinuity within the 3D contour. Various studies have already used The AS algorithm for 3D reconstruction, canopy extraction, LA, and crown biomass estimation [50,51].

2.4.3. LA Calculation with TLS Data

The theoretical basis of indirect LAI measurement is the Beer–Lambert law, also known as Beer’s law. It was originally used to describe the attenuation of light in uniform mediums and further extended to the light interception of homogeneous canopies [52]. The classic relationship between the LAI and gap fraction in a specific zenith angle was established as follows:

$$P(\theta) = e^{-G(\theta) \times LAI / \cos(\theta)} \quad (1)$$

where $P(\theta)$ is the gap probability in the observation zenith angle θ and $G(\theta)$ is the extinction coefficient, expressed as the blade projection along the scanning direction. In most studies, $G(\theta)$ is set to 0.5 based on the $G(\theta)$ value of a spherical model: when $\theta = 57.5^\circ$, the effect of the leaf angle distribution on the extinction coefficient is minimal [53].

After the voxelization of TLS data, we first extracted the gap fraction (GF) at each layer in the Z direction following Equation (2):

$$GF_i = \frac{N0_i}{Nt_i} \quad (2)$$

where GF_i represents the gap fraction at i th layer, $N0_i$ and Nt_i stand for the number of voxels classified as (0) and the total number of voxels (both empty and non-empty), respectively. Then, based on the definition of LAI [54], the LAI and LA at individual scale can be calculated as

$$LAI_i = -\frac{\cos(\theta_i) \times \ln(GF_i)}{G(\theta)} \quad (3)$$

$$LA = \sum_{i=1}^n LAI_i \times A \quad (4)$$

$\cos(\theta_i)$ refers to the zenith angle at i th layer, LAI_i denotes LAI at i th layer, and A is the crown projection area.

Several instruments were developed based on this theory for indirect LAI measurement, and promising results were achieved [55]. However, the issue of the clumping effect was found to have a considerable impact on this theory when applied to other vegetation with complex structures. As an alternative, we applied the path length distribution method as a non-voxel-based approach to calculate LA (LA_PLD).

The path length distribution is defined as the probability function of the path length within the tree crown that corresponds to the gap probability measurement. The path length is defined as the length of a ray passing through a tree crown, and LAI can be expressed as

$$LAI_{PATH} = \int_0^1 (\rho \times l_{max}) \times \cos(\theta) \times l_r \times P_{lr}(l_r) d(l_r) \quad (5)$$

where ρ is the foliage area volume density, l_r , and l_{max} denote the maximum and relative path length along the transect. The path length distribution function $P_{lr}(l_r)$ meets the following condition:

$$\int_0^1 P_{lr}(l_r) d(l_r) = 1 \quad (6)$$

More detailed information on the path length distribution method can be found in Hu et al. [56].

2.5. Statistical Analysis

As stated in the introduction, we applied ordinary least squares (OLS) regressions and nonlinear least squares (NLS) regressions for biomass estimation using field-measured parameters to address our first objective. OLS regressions were also applied to evaluate the biomass estimation accuracy using voxel- and non-voxel-based approaches. Three parameters were used for evaluating the goodness of fit and prediction accuracy, namely the coefficient of determination (R^2), root mean squared error (RMSE), and relative RMSE (rRMSE), which were expressed using the following Equations (7)–(9):

$$R^2 = 1 - \frac{\sum_{i=1}^n (M_i - P_i)^2}{\sum_{i=1}^n (M_i - M_{mean})^2} \quad (7)$$

$$RMSE = \sqrt{\frac{\sum_{i=1}^n (M_{mean} - P_i)^2}{n}} \quad (8)$$

$$rRMSE = \frac{RMSE}{M_{mean}} \times 100\% \quad (9)$$

$$MAE = \frac{\sum_{i=1}^n |P_i - M_i|}{n} \quad (10)$$

where M_i and P_i denote the i th measured and predicted parameters, respectively. M_{mean} represents the mean value of a measured parameter, and n equals the sample size. Models showing higher values of R^2 and lower values of RMSE and rRMSE were considered optimal.

To evaluate the accuracy of LA calculation and total biomass estimation using the non-voxel-based approach, we applied OLS regression using the calculated and measured parameters, which theoretically should be close to the function of $y = x$; therefore, the regression function with a slope closer to 1 and intercept near 0 denotes better calculated result.

In the process of estimating stem biomass with derived stem volume, we applied leave-one-out cross-validation (LOOCV) for evaluation. The mean absolute error (MAE) was applied to evaluate the prediction accuracy, which was expressed in the following Equation (10). Statistical analysis was conducted on the R statistical package.

Correlation plots were applied for methods comparison using Pearson's r as the correlation coefficient, with measured, inventory-based, voxel-, and non-voxel-based parameters listed in the plots from top to bottom, respectively. Larger circles and more red-inclined colors indicated a higher correlation between the two parameters. Parameters with correlation coefficients < 0.5 are represented in black.

3. Results

3.1. Biomass Estimation Using Field-Measured Parameters

We conducted OLS between the five measured parameters and oven-dried biomass; the results are shown below (Table 2). Detailed information on the OLS and NLS regression is presented in Table S1.

Table 2. Biomass estimation with inventory data.

Species	Measured Biomass	Parameters	R^2 , $R^2_{Adjusted}$	RMSE (g)	rRMSE %	p -Value
<i>Grewia biloba</i> $n = 15$	Total biomass	Crown Area	0.61, 0.58	38.11	44.62	<0.001
		Crown Length	0.51, 0.48	42.46	49.71	0.003
		Crown Width	0.61, 0.58	38.09	44.60	<0.001
		Height	0.80, 0.79	26.93	31.53	<0.001
		Basal Diameter	0.25, 0.19	52.61	61.60	0.056
		Basal Diameter, height	0.32, 0.26	50.30	58.89	0.029
<i>Vitex negundo</i> $n = 15$	Total biomass	Crown Area	0.47, 0.42	14.18	62.03	0.005
		Crown Length	0.57, 0.54	12.67	55.42	<0.001
		Crown Width	0.27, 0.21	16.62	72.70	0.045
		Height	0.63, 0.61	11.76	51.44	<0.001
		Basal Diameter	0.11, 0.04	18.39	80.44	0.229
		Basal Diameter, height	0.10, 0.03	18.52	81.01	0.258
<i>Diospyros lotus</i> $n = 15$	Total biomass	Crown Area	0.88, 0.87	16.61	27.11	<0.001
		Crown Length	0.76, 0.74	23.74	38.74	<0.001
		Crown Width	0.75, 0.73	24.03	39.22	<0.001
		Height	0.83, 0.81	12.50	20.40	<0.001
		Basal Diameter	0.11, 0.04	46.16	75.34	0.231
		Basal Diameter, height	0.09, 0.02	46.70	76.22	0.288
NLS regression	Total biomass	Crown Area	0.91, 0.90	12.38	20.21	<0.001

Vegetation height yielded the highest accuracy among all the parameters, with the highest R^2 and lowest RMSE and rRMSE values in the three species using OLS regression, whereas the basal diameter could not achieve satisfying results, with a p -value greater than 0.01. The biomass of *Diospyros lotus* can be estimated with considerable accuracy aside from the basal diameter, while the estimation of the two shrub species did not yield adequate results, with most of the R^2 values approximately or below 0.6 and p -values higher than 0.01. In addition, the estimation results of *Diospyros lotus* were the highest in general, with all the parameters yielding an rRMSE below 40% except for basal diameter. In contrast, nearly all the rRMSE values were higher than in the two shrub species (except when estimating the biomass of *Grewia biloba* with height). The NLS regression results using the crown area (R^2 equaled 0.48–0.91) were more accurate than regarding the basal diameter and height (R^2 equaled 0.03–0.26) for the three studied species and can provide valid estimation results for *Grewia biloba* and *Diospyros lotus* (p -value below 0.001).

3.2. Biomass Estimation Using Voxelization Approaches

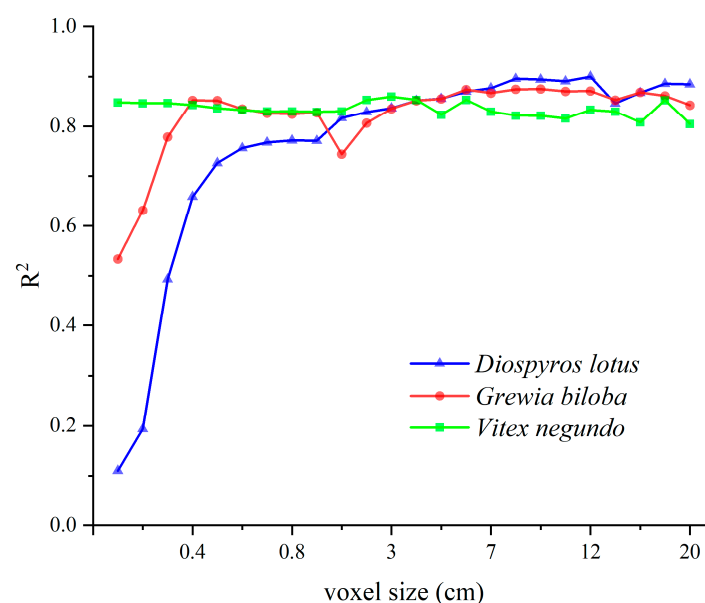
In the process of estimating biomass using the voxel-based approach, we employed two schemes as described in Section 2.4.1, and the results are shown below (Table 3). Detailed information on the OLS regression is presented in Figures S1–S3.

Table 3. Voxel-based biomass estimation model.

Species	Measured Biomass	Parameters	R ² , Adjusted R ²	RMSE (g)	rRMSE %	p-Value
<i>Grewia biloba</i> n = 15	Total biomass	Plant volume	0.87, 0.86	19.16	22.43	<0.001
	Leaf biomass	LA	0.86, 0.85	3.76	25.37	<0.001
	Stem biomass	Stem volume	0.89, 0.87	17.62	24.96	<0.001
	Total biomass	Stem volume, LA	0.91, 0.90	18.18	21.29	<0.001
<i>Vitex negundo</i> n = 15	Total biomass	Plant volume	0.86, 0.84	6.43	28.13	<0.001
	Leaf biomass	LA	0.65, 0.57	1.82	40.80	0.014
	Stem biomass	Stem volume	0.82, 0.79	7.37	40.05	<0.001
	Total biomass	Stem volume, LA	0.86, 0.85	7.76	33.94	<0.001
<i>Diospyros lotus</i> n = 15	Total biomass	Plant volume	0.93, 0.92	21.03	34.32	<0.001
	Leaf biomass	LA	0.57, 0.50	6.36	42.19	0.013
	Stem biomass	Stem volume	0.93, 0.92	11.06	23.94	<0.001
	Total biomass	Stem volume, LA	0.96, 0.94	11.92	19.45	<0.001

The two voxelization schemes both achieved accurate estimation results compared to the inventory parameters, especially in the two shrub species, with the R² of *Grewia biloba* increasing from 0.19–0.79 (Table 2) to 0.86–0.90 (Table 3) and RMSE decreasing from 26.93–52.16 g to 18.18–19.16 g and the R² of *Vitex negundo* increasing from 0.02–0.61 to 0.84–0.85 and RMSE decreasing from 11.76–19.39 g to 6.43–7.76 g. Moreover, rRMSE decreased from 31.53–61.60% to 21.29–22.43% for *Grewia biloba* and 51.44–80.44% to 28.13–33.94% for *Vitex negundo*. However, the result using the inventory approach with height for biomass estimation of *Diospyros lotus* (20.40%) was approximate to that of the voxel-based approach (19.45%). Of all three studied species, only the estimation result of *Vitex negundo* using scheme two was lower than scheme one, with the rRMSE values equaling 33.94% and 28.13%, respectively.

We then studied the estimation accuracy in different voxel sizes for the three low-statured vegetations (Figure 6). R² of both *Grewia biloba* and *Diospyros lotus* experienced an uptrend when voxel size increased from 0.2 cm, then reached the inflection point when voxel size equaled 0.5 cm and 0.7 cm, respectively. In contrast, *Vitex negundo* did not share a similar trend. Different voxel sizes led to various results, with the maximum R² differences equaling 0.4 for *Grewia biloba*, 0.08 for *Vitex negundo*, and 0.8 for *Diospyros lotus*, respectively.

**Figure 6.** Biomass estimation accuracy under different species and voxel sizes.

It is worth noting that scheme (b) performed slightly better than scheme (a) (R^2 ranging from 0.84–0.92 to 0.85–0.94). Therefore, in the following study, we only applied scheme (b) to evaluate the feasibility of the non-voxel approach in estimating understory biomass (Table 3).

3.3. Non-Voxel-Based Approach to Estimate Leaf, Stem, and Total Biomass

The estimation accuracy of LA obtained using the path length distribution method was better than that of the voxel-based method (Figure 7a), with R^2 and RMSE equal to 0.94 and 582.05 cm^2 (Figure 7b). In addition, scatter points of LA_PLD were distributed closer to the 1:1 line, indicating a closer calculation to the measured LA. LA_VGF, on the other hand, did not achieve similar accuracy.

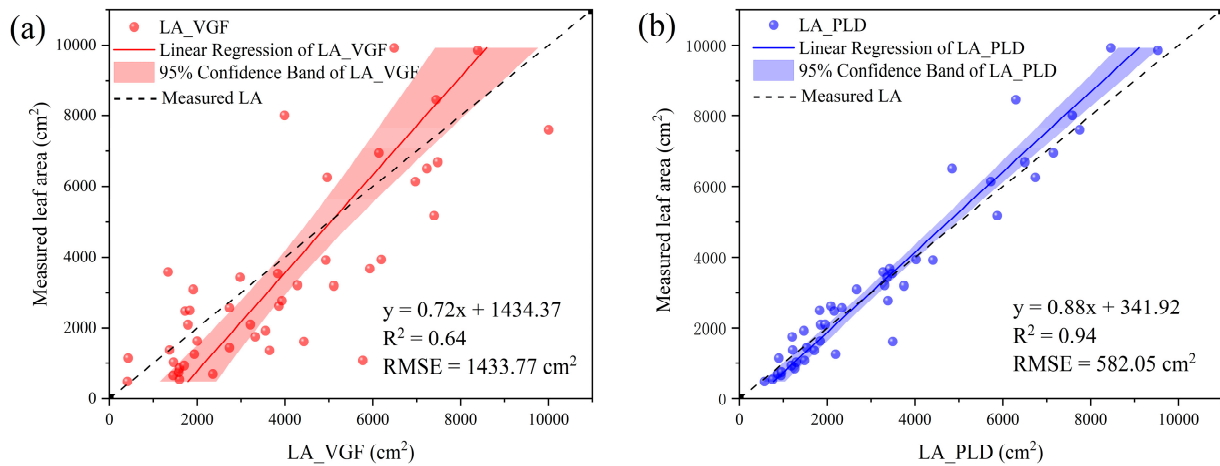


Figure 7. Leaf area estimation using (a) voxel-based approach and (b) non-voxel-based approach.

CH and AS algorithms were applied to acquire the volumes of the forty-five samples using leaf-off PCD, and stem biomass density was calculated by dividing the measured stem biomass by volume. We hypothesized that the stem biomass density of samples from the same species should be approximated. The box chart below (Figure 8) demonstrates the calculation results with samples grouped by species and algorithms. The results obtained using the preferable algorithm should be more clustered in distribution, with more samples falling within the interquartile range (IQR), and would be utilized in the estimation of stem biomass.

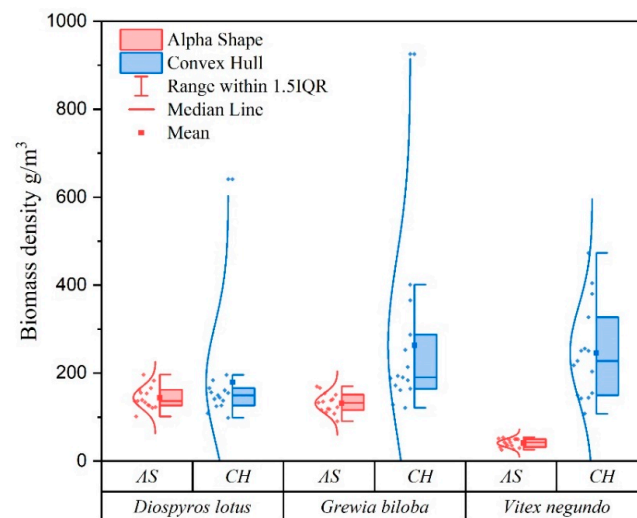


Figure 8. Biomass density calculated using AS and CH algorithms.

The stem biomass density of the *Vitex negundo* samples illustrated a large variance of approximately 200 g/m³ based on the two algorithms, unlike the other two species. Apart from that, we discovered that, among the biomass densities obtained through the two volume algorithms, the AS algorithm yielded more stable results, with lower differences in changes within species (the variances regarding all three species are within 200 g/m³). In contrast, the results of the CH algorithm featured a more dispersed distribution, with differences within species reaching 900 g/m³ for *Grewia biloba* and 500 g/m³ for *Vitex negundo* and *Diospyros lotus*, three to four times higher than the results calculated using the AS algorithm. Therefore, we only utilized volumes derived using the AS algorithm in the process of estimating stem biomass using OLS regression.

We applied LOOCV to evaluate the accuracy of regression between stem biomass and volume (Table 4). Stem biomass can be regressed and predicted well using AS-derived volume with R² above 0.9 and MAE below 10 g for all three species. Estimation accuracy was improved compared to the voxel-based approach, especially in the case of *Vitex negundo*, with rRMSE decreasing from 40.05% (Table 3) to 24.02%.

Table 4. Cross-validation between stem biomass and stem volume derived using the AS algorithm.

Species	Parameters	Validation Method	RMSE (g)	rRMSE%	R ²	MAE (g)
<i>Grewia biloba</i>	Stem biomass and volume	LOOCV	11.22	15.90	0.95	9.23
<i>Vitex negundo</i>			4.42	24.02	0.92	3.47
<i>Diospyros lotus</i>			8.15	17.64	0.96	6.50

The total biomass estimation was aggregated using regression equations acquired from the leaf (Figure 9a) and stem biomass (Figure 9b) estimation via non-voxel-based approaches (Figure 9c). The estimation accuracy of leaf biomass using this method was relatively high, with R² values of 0.89, 0.72, and 0.93 and RMSE values of 3.22 g, 1.48 g, and 2.40 g, respectively. Although the estimation result of *Vitex negundo* was lower than the other two species, there was still an improvement compared to the voxel-based method (R² = 0.57; RMSE = 1.82 g). The three studied species displayed promising results of R² equaling 0.95, 0.93, and 0.96, and RMSE values equaling 11.27, 4.23, and 7.79 g. Compared with the results obtained using the voxel-based approach, all three species reached a higher biomass estimation accuracy, especially in the case of *Vitex negundo*, with the regression R² increasing from 0.85 to 0.95. Detailed information about the fitting equations can be found in Table S2.

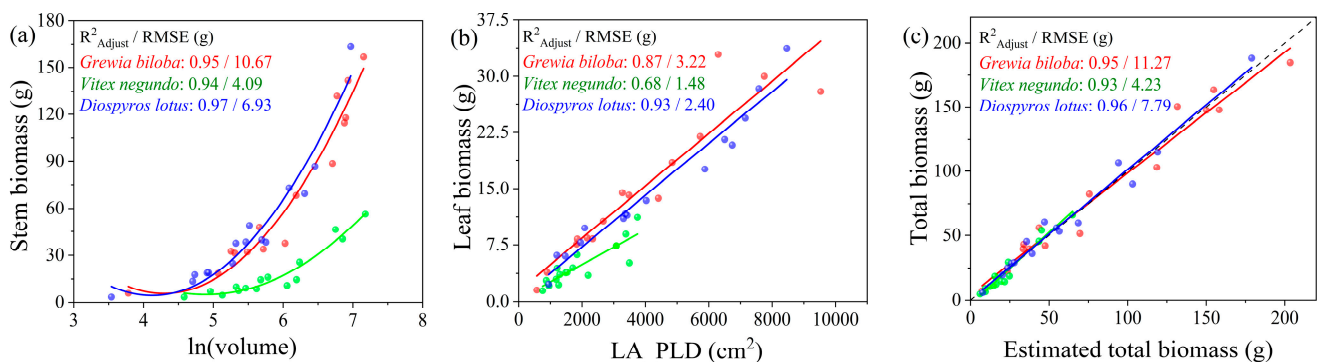


Figure 9. Estimation of (a) leaf biomass, (b) stem biomass, and (c) total biomass using non-voxel-based approaches, with *Grewia biloba*, *Vitex negundo*, and *Diospyros lotus* represented by red, green, and blue dots and lines, respectively. The 1:1 dashed line indicates measured total biomass.

3.4. Comparison of Biomass Estimation Using Inventory, Voxel-, and Non-Voxel-Based Approaches

We compared the inventory data versus TLS-based methods by species using correlation plots. In the example of *Grewia biloba* (Figure 10, abbreviations in Table 5), the

correlation between the basal diameter and total biomass was ≤ 0.5 , making it the weakest predictive factor among inventory parameters, whereas the correlation between height and total biomass was 0.9, being the highest.

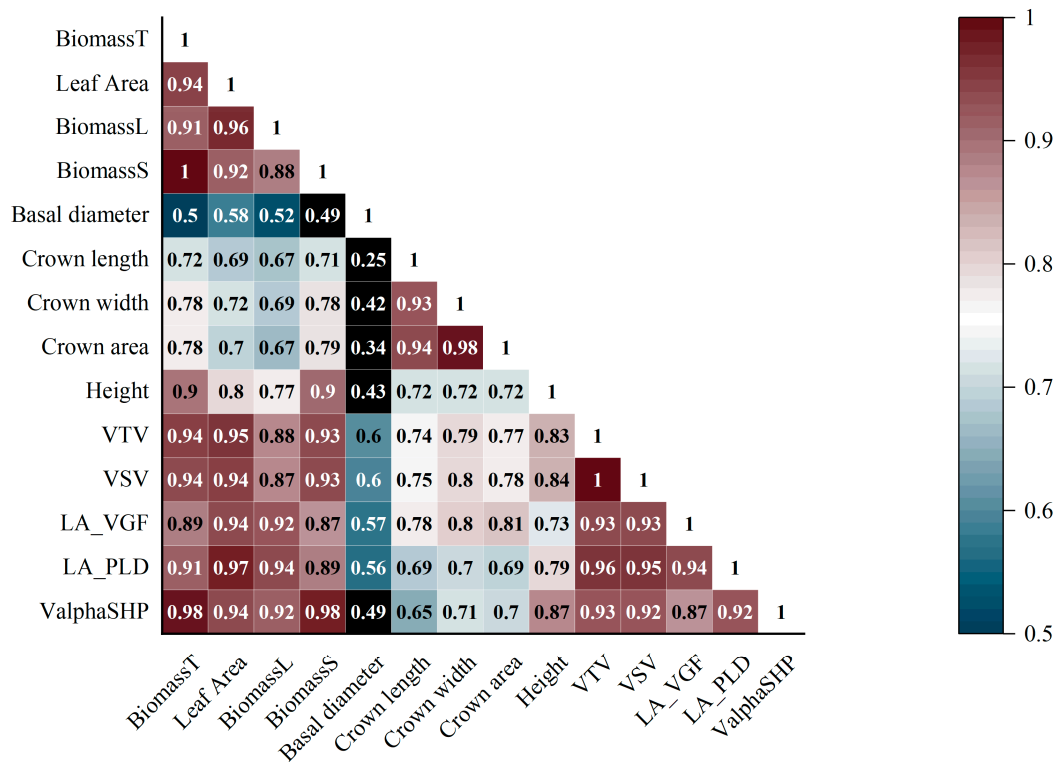


Figure 10. Correlation map of measured biomass and LA and parameters used in three biomass estimation approaches (in the case of *Grewia biloba*) using Pearson’s r. The results of the other two species are similar and are shown in Figures S4 and S5.

Table 5. Elaboration of abbreviations in the correlation maps.

Abbreviation	Elaboration
BiomassT, BiomassL, BiomassS	Measured total, leaf, and stem biomass
VTV, VSV	Total and stem volume derived from voxels
LA_VGF, LA_PLD	Leaf area estimated from voxels and path length distribution method
ValphaSHP	Stem volume derived from AS algorithms

A stronger correlation can be observed with measured biomass and TLS-derived parameters in contrast with field-measured parameters (the correlations between VSV, ValphaSHP, and stem biomass, and the correlations between LA_VGF, LA_PLD, LA, and leaf biomass were all greater than 0.9). After distinguishing stems and leaves, the correlations between the parameters extracted using the non-voxel-based approach and the corresponding measured data were also slightly higher than those extracted using the voxel-based-approach, specifically manifested as $R_{\text{BiomassL-LA_PLD}} (0.94) > R_{\text{BiomassL-LA_VGF}} (0.92)$, $R_{\text{BiomassS-ValphaSHP}} (0.98) > R_{\text{BiomassS-VSV}} (0.93)$. Among the three methods, the parameters extracted using the non-voxel-based approach have the highest correlation with the corresponding measured data, followed by the parameters extracted using the voxel-based approach. Inventory parameters have the lowest correlation with the measured data.

4. Discussion

4.1. Performance of Inventory and TLS-Based Approaches

Among the three understory species, only *Diospyros lotus*, a low-statured tree, yielded accurate biomass estimation results with field-measured parameters (R^2 ranging from 0.73

to 0.87; basal diameter not included) compared to the remaining shrub species (R^2 ranging from 0.21 to 0.58; basal diameter not included), with only one exception when estimating the biomass of *Grewia biloba* with height ($R^2 = 0.79$). The basal diameter, a parameter most frequently used in other studies, however, did not yield valid results, with R^2 approximated at or below 0.3 in all three species using both OLS and NLS regressions, contradicting the existing studies [57,58], which could possibly be due to the following reasons: (a) the existing allometric models for plant species were developed for large tree individuals harvested in managed forests for merchantable volume; thus, the parameters in the existing models may not be appropriate for the quantification of AGB of short-stature shrubs growing in unmanaged ecosystems [59]. (b) There is a lack of regionally applicable allometric models for understory vegetation located in the Yanshan Mountains; thus, the optimal parameter(s) for biomass estimation using inventory approaches in our study remained unclear. Both OLS and NLS regressions using crown area provided accurate estimation results for the AGB of *Diospyros lotus* (R^2 equaled 0.88 and 0.91, respectively). In contrast, the estimation results of the two shrub species were less satisfying (R^2 equaled 0.47 to 0.61), indicating that the relationship between crown area and biomass may have been affected by the greater heterogeneity in terms of species diversity; competition between neighboring trees can influence the crown structure, leading to variability in aboveground biomass [60]. Kalita et al. [61] also suggested refining allometric equations by adding height and crown area to the equations, which could possibly further improve the accuracy for biomass estimation of *Diospyros lotus* as height and crown area were proven to be better predictor variables in our study. However, the method for AGB estimation of shrub species required further improvement. It is worth noting that, in a study that conducted the targeting of three similar-condition low-statured shrubs and trees, Flade et al. [62] established allometric equations using 1D (stem length and basal diameter), 2D (cross-sectional area basal), and 3D (volume) parameters, respectively. They discovered that volume obtained in field measurement provided the highest accuracy of estimation, whereas estimation using other parameters failed to deliver accurate results, with R^2 values all below or approximately 0.5.

Between the two biomass estimation schemes, separating stems and leaves and estimating the corresponding portion of biomass separately using stem volume and LA yielded slightly better estimation accuracy (Table 3) as stems and leaves of the same species have various biomass densities. In addition, there is a strong correlation between leaf area and leaf biomass [13]; thus, separating the two vegetation components could theoretically lead to better estimation results. By collecting leaves during in situ measurements, we further reduced occlusion within quadrats, which helped to acquire more detailed scanning of the target plants, thus minimizing information loss during voxelization.

4.2. Comparison of the Voxel-Based and Non-Voxel-Based Approach

The voxel-based approach obtained considerable results in estimating plant and stem biomass for the three species (Table 3). However, we discovered that, with different species, even different components of the same species, the optimal voxel size varies accordingly (the optimal voxel sizes for estimating leaf, stem, and plant biomass are 9 cm, 2 cm, and 12 cm, respectively, in the case of *Diospyros lotus*, Figure S3). Since there are no previous studies regarding understory biomass estimation in the Yanshan Mountains, we tested voxel sizes ranging from 0.2 cm to 20 cm to reveal the optimal voxel size for deriving aboveground biomass for three different vegetation types. The selection of the optimal voxel size played an essential role in estimating biomass. The optimal voxel size represents a compromise among factors, including the point spacing, pulse diameter, and occlusion rate of voxels [38,39,42]. When estimating understory biomass, the optimal voxel size should be small enough to capture detailed structural information and exclude pores within the canopy and stems yet large enough for the ratio of an empty voxel (0) to remain minimum to increase estimation accuracy [63]. In our study, the optimal voxel sizes for the three species are 9 cm, 6 cm, and 12 cm, respectively (Figures S1–S3), which supported the hypothesis that optimal voxel size for characterizing individual vegetation structure

information using voxels may range from 5 cm to 20 cm [42]. However, other studies may hold contradictory results, implying that the error magnitudes for the investigated point cloud metrics and plant metrics are the lowest with scaled voxels or with the smallest fixed-sized voxels (2 cm) [64]. In contrast, Menéndez et al. [44] denoted that a large voxel grid of 25 cm (low number of voxels) is more efficient than finer resolutions of voxelization. Determining the optimal voxel size based on features of PCD and mathematical approaches should be a focus of concern.

In contrast with the voxel-based approach, we discovered that the non-voxel-based method provided better results in leaf and stem biomass estimation (Figure 9c). In addition, our study proved the feasibility of the path length distribution method in calculating LA of understory vegetation at individual scale, performing better than the voxel-based approach. The clumping effect is widely recognized as the cause affecting the accuracy of LAI calculation as Beer's law is utilized under the hypothesis that leaves are randomly spatially distributed, whereas, in reality, leaves are generally clumped within canopies. Thus, the clumping index is widely proposed for accurate LAI and LA estimation [65]. It is a variable parameter that changes with observation direction, location, scale, and season [66]. However, the spatial heterogeneity caused by various path lengths within canopies has not been considered using a simple clumping index. The recently proposed path length distribution model [67] provides a novel solution for quantifying the clumping effect. The path length is directly related to the gap probability in Beer's law, which can be utilized to establish a physical model to connect average gap probability with LAI using path length distribution. As a relatively new method, its main difference from the voxel-based method is quantifying gap fraction using path length, providing the advantages of considering tree crown shapes and tree height distributions, which are essential for modeling the 3D spatial distribution of leaves and within-crown clumping [53]. The AS method was also introduced in our study for deriving stem volume as a non-voxel-based approach. The parameter α is used to determine the level of detail of the obtained triangulation, which controls the fineness of the generated polyhedron, directly affecting the surface reconstruction results [68,69]. In this study, α was set to a constant of 0.05 for the following reasons: (a) when calculating canopy volumes and structural parameters of fruit trees, Liu et al. [49] suggested that the canopy structure was expressed in a detailed manner, which expresses the canopy topological structure and degree of density when α was set to 0.05; and (b) the stem biomass density shown in Figure 8 indicated a smaller difference within species calculated using the AS algorithm, which was more in line with our hypothesis that samples from the same species should possess biomass density of low divergence. Our cross-validation results support that statement (Table 4).

In this study, we acquired stem PCD by collecting leaves during field observation and conducted scanning in leaf-off conditions. However, many studies have proven the feasibility of separating leaves and stems of understory vegetation using PCD alone, which would significantly reduce labor force and time, rendering our non-voxel-based approach more practical in vegetation monitoring. For instance, Arslan et al. [31] implemented the neural network segmentation (NNS) method for wood removal in the LAI calculation process, which involved neural network-supported classification to perform a binary classification of PCD, successfully subsampling PCD into leaf and stem point clouds. Olsoy et al. [70] employed a laser reflectance value as a threshold for separating wood and leaf points when calculating the LAI of Arctic sagebrush, where points with a reflectance value below the threshold are classified as green or photosynthetically active points.

TLS metrics permit a significant improvement in estimates obtained through allometric biomass models since these models predict population averages for individuals with the same characteristics at individual scale [71]. Many studies have now combined TLS and ALS for quantifying and plotting biomass of low-statured vegetation at stand scale [72–75]. However, few studies have committed to mapping forest understory biomass at stand scale with ALS, possibly due to occlusion from the canopy and ALS's low point density trait, posing challenges in calibrating TLS data and ALS data for stand scale understory

biomass plotting. Future research initiatives should focus on testing the results obtained in this study on other understory species in the Yanshan Mountains and achieving biomass mapping on both overstory and understory biomass, thus acquiring full vertical structural information about forests at stand scale. In addition, understory biomass was found to be predominantly driven by light and nitrogen availability, and overstory characteristics could be a potential indicator of understory biomass stock in mature temporal forests [76,77]. Therefore, discovering relationships between overstory characteristics and understory biomass could help to calibrate ALS data and TLS data in forests, thus achieving understory biomass mapping at stand scale and helping to quantify its effect on local nutrient cycling and its response to global change [78].

5. Conclusions

This study utilized high-resolution PCD obtained using TLS and achieved biomass estimation of three common understory species in the Yanshan Mountains with a non-voxel-based approach combining the path length distribution method and the AS algorithm. The biomass estimation results were compared with existing LiDAR-based biomass estimation methods and inventory parameters with measured biomass from provided destructive sampling references. The results obtained in this work highlighted the great potential of TLS to replace field measurement in understory biomass estimation. On the one hand, TLS permits the quantification and inclusion in the models of certain metrics that cannot easily be assessed through inventories, including volume and LA. On the other hand, our non-voxel-based approach successfully bypassed the objectively set parameter, voxel size, during voxelization, which could significantly affect accuracy with different set values.

In contrast with low-statured trees, biomass estimation using field-measured parameters yielded lower accuracy in the two shrub species ($R^2 = 0.19\text{--}0.79$ and $0.02\text{--}0.61$), showing that, unlike in previous studies [79,80], inventory parameters may not be suited for estimating shrub biomass in the Yanshan Mountains. A more precise estimate could be obtained when estimating the biomass of stems and leaves separately from volume–biomass fitting of the entire shrub with the voxel-based approach using TLS data (with R^2 values all equal or approximate to 0.9). However, voxel sizes can have a significant impact on estimation accuracy. The path length distribution method acquired a higher calculation accuracy of LA than the voxel-based approach, thus leading to a better estimation result of leaf biomass (the results of *Diospyros lotus* improved most dramatically with R^2 increased from 0.5 to 0.9). When estimating stem biomass, the AS algorithm yielded a stem biomass density more in line with our hypothesis of “samples from a same species possess biomass density of low divergence”, which in turn resulted in an accurate estimation of stem biomass (with R^2 values all above 0.9 for the three species).

Supplementary Materials: The following supporting information can be downloaded at <https://www.mdpi.com/article/10.3390/rs16061060/s1>; Figure S1: Voxel-based approach for estimating biomass of *Grewia biloba* with optimal voxel sizes; Figure S2: Voxel-based approach for estimating biomass of *Vitex negundo* with optimal voxel sizes; Figure S3: Voxel-based approach for estimating biomass of *Diospyros lotus* with optimal voxel sizes; Figure S4: Correlation map of measured biomass and parameters used in three biomass estimation approaches (*Vitex negundo*); Figure S5: Correlation map of measured biomass and parameters used in three biomass estimation approaches (*Diospyros lotus*). Table S1: Fitting equations of biomass estimation using inventory approach; Table S2: Fitting equations of biomass estimation using non-voxel-based approach.

Author Contributions: Conceptualization, Y.L. and H.N.; methodology and software, R.H., Y.X. and Y.L.; data collection, Y.L. and Z.P.; data process and analysis, Y.L.; writing—original draft preparation, Y.L.; writing—review and editing, H.N. and R.H.; supervision, Z.C.; project administration, H.N. and Z.C.; funding acquisition, H.N. All authors have read and agreed to the published version of the manuscript.

Funding: This research was supported by the Science and Technology Basic Resources Survey: Aboveground biomass of Yanshan–Taihang Mountains (2022FY100102-02) and by the Fundamental Research Funds for the Central Universities.

Data Availability Statement: Data available upon request. The data are not publicly available due to legal reasons.

Acknowledgments: We would like to thank and acknowledge volunteers for participating in leaf area measurements and the reviewers and editors who contributed to the final version of this manuscript.

Conflicts of Interest: The authors declare no conflicts of interest.

References

- MacFarlane, D.W. A generalized tree component biomass model derived from principles of variable allometry. *For. Ecol. Manag.* **2015**, *354*, 43–55. [[CrossRef](#)]
- Burt, A.; Vicari, M.B.; da Costa, A.C.L.; Coughlin, I.; Rowland, L.; Disney, M. New insights into large tropical tree mass and structure from direct harvest and terrestrial lidar. *R. Soc. Open Sci.* **2021**, *8*, 201458. [[CrossRef](#)] [[PubMed](#)]
- Kukenbrink, D.; Gardi, O.; Morsdorf, F.; Thurig, E.; Schellenberger, A.; Mathys, L. Above-ground biomass references for urban trees from terrestrial laser scanning data. *Ann. Bot.* **2021**, *128*, 709–724. [[CrossRef](#)] [[PubMed](#)]
- Dixon, R.K.; Solomon, A.M.; Brown, S.; Houghton, R.A.; Trexler, M.C.; Wisniewski, J. Carbon pools and flux of global forest ecosystems. *Science* **1994**, *263*, 185–190. [[CrossRef](#)]
- Guo, Z.; Fang, J.; Pan, Y.; Birdsey, R. Inventory-based estimates of forest biomass carbon stocks in China: A comparison of three methods. *For. Ecol. Manag.* **2010**, *259*, 1225–1231. [[CrossRef](#)]
- Chambers, J.Q.; Asner, G.P.; Morton, D.C.; Anderson, L.O.; Saatchi, S.S.; Espirito-Santo, F.D.B.; Palace, M.; Souza, C., Jr. Regional ecosystem structure and function: Ecological insights from remote sensing of tropical forests. *Trends Ecol. Evol.* **2007**, *22*, 414–423. [[CrossRef](#)]
- Le Noe, J.; Erb, K.-H.; Matej, S.; Magerl, A.; Bhan, M.; Gingrich, S. Altered growth conditions more than reforestation counteracted forest biomass carbon emissions 1990–2020. *Nat. Commun.* **2021**, *12*, 6075. [[CrossRef](#)]
- Yarie, J. The Role of Understory Vegetation in the Nutrient Cycle of Forested Ecosystems in the Mountain Hemlock Biogeoclimatic Zone. *Ecology* **1980**, *61*, 1498–1514. [[CrossRef](#)]
- Misson, L.; Baldocchi, D.D.; Black, T.A.; Blanken, P.D.; Brunet, Y.; Yuste, J.C.; Dorsey, J.R.; Falk, M.; Granier, A.; Irvine, M.R.; et al. Partitioning forest carbon fluxes with overstory and understory eddy-covariance measurements: A synthesis based on FLUXNET data. *Agric. For. Meteorol.* **2007**, *144*, 14–31. [[CrossRef](#)]
- Moore, P.T.; Van Miegroet, H.; Nicholas, N.S. Relative role of understory and overstory in carbon and nitrogen cycling in a southern Appalachian spruce-fir forest. *Can. J. For. Res.* **2007**, *37*, 2689–2700. [[CrossRef](#)]
- Benjamin, B.C.; Hudak, A.T.; Meddens, A.J.H.; Hawbaker, T.J.; Briggs, J.S.; Kennedy, R.E. Prediction of Forest Canopy and Surface Fuels from Lidar and Satellite Time Series Data in a Bark Beetle-Affected Forest. *Forests* **2017**, *8*, 322.
- White, J.C.; Coops, N.C.; Wulder, M.A.; Vastaranta, M.; Hilker, T.; Tompalski, P. Remote Sensing Technologies for Enhancing Forest Inventories: A Review. *Can. J. Remote Sens.* **2016**, *42*, 619–641. [[CrossRef](#)]
- Greaves, H.E.; Vierling, L.A.; Eitel, J.U.H.; Boelman, N.T.; Magney, T.S.; Prager, C.M.; Griffin, K.L. Estimating aboveground biomass and leaf area of low-stature Arctic shrubs with terrestrial LiDAR. *Remote Sens. Environ.* **2015**, *164*, 26–35. [[CrossRef](#)]
- Demol, M.; Verbeeck, H.; Gielen, B.; Armston, J.; Burt, A.; Disney, M.; Duncanson, L.; Hackenberg, J.; Kukenbrink, D.; Lau, A.; et al. Estimating forest above-ground biomass with terrestrial laser scanning: Current status and future directions. *Methods Ecol. Evol.* **2022**, *13*, 1628–1639. [[CrossRef](#)]
- Calders, K.; Newnham, G.; Burt, A.; Murphy, S.; Raunonen, P.; Herold, M.; Culvenor, D.; Avitabile, V.; Disney, M.; Armston, J.; et al. Nondestructive estimates of above-ground biomass using terrestrial laser scanning. *Methods Ecol. Evol.* **2015**, *6*, 198–208. [[CrossRef](#)]
- Huff, S.; Ritchie, M.; Temesgen, H. Allometric equations for estimating aboveground biomass for common shrubs in northeastern California. *For. Ecol. Manag.* **2017**, *398*, 48–63. [[CrossRef](#)]
- Colgan, M.S.; Asner, G.P.; Swemmer, T. Harvesting tree biomass at the stand level to assess the accuracy of field and airborne biomass estimation in savannas. *Ecol. Appl.* **2013**, *23*, 1170–1184. [[CrossRef](#)]
- Quint, T.C.; Dech, J.P. Allometric models for predicting the aboveground biomass of Canada yew (*Taxus canadensis* Marsh.) from visual and digital cover estimates. *Can. J. For. Res.* **2010**, *40*, 2003–2014. [[CrossRef](#)]
- Chen, Y.; Cai, X.A.; Zhang, Y.; Rao, X.; Fu, S. Dynamics of Understory Shrub Biomass in Six Young Plantations of Southern Subtropical China. *Forests* **2017**, *8*, 419. [[CrossRef](#)]
- Asner, G.P.; Mascaro, J.; Anderson, C.; Knapp, D.E.; Martin, R.E.; Kennedy-Bowdoin, T.; van Breugel, M.; Davies, S.; Hall, J.S.; Muller-Landau, H.C.; et al. High-fidelity national carbon mapping for resource management and REDD+. *Carbon Balanc. Manag.* **2013**, *8*, 7. [[CrossRef](#)]
- Du, L.; Pang, Y.; Wang, Q.; Huang, C.; Bai, Y.; Chen, D.; Lu, W.; Kong, D. A LiDAR biomass index-based approach for tree- and plot-level biomass mapping over forest farms using 3D point clouds. *Remote Sens. Environ.* **2023**, *290*, 113543. [[CrossRef](#)]

22. Wang, F.; Sun, Y.; Jia, W.; Li, D.; Zhang, X.; Tang, Y.; Guo, H. A Novel Approach to Characterizing Crown Vertical Profile Shapes Using Terrestrial Laser Scanning (TLS). *Remote Sens.* **2023**, *15*, 3272. [[CrossRef](#)]
23. Lefsky, M.A.; Cohen, W.B.; Harding, D.J.; Parker, G.G.; Acker, S.A.; Gower, S.T. Lidar remote sensing of above-ground biomass in three biomes. *Glob. Ecol. Biogeogr.* **2002**, *11*, 393–399. [[CrossRef](#)]
24. Kato, A.; Moskal, L.M.; Schiess, P.; Swanson, M.E.; Calhoun, D.; Stuetzle, W. Capturing tree crown formation through implicit surface reconstruction using airborne lidar data. *Remote Sens. Environ.* **2016**, *113*, 1148–1162. [[CrossRef](#)]
25. Drake, J.B.; Dubayah, R.O.; Clark, D.B.; Knox, R.G.; Blair, J.B.; Hofton, M.A.; Chazdon, R.L.; Weishampel, J.F.; Prince, S. Estimation of tropical forest structural characteristics using large-footprint lidar. *Remote Sens. Environ.* **2002**, *79*, 305–319. [[CrossRef](#)]
26. Glenn, N.F.; Spaete, L.P.; Sankey, T.T.; Derryberry, D.R.; Hardegree, S.P.; Mitchell, J.J. Errors in LiDAR-derived shrub height and crown area on sloped terrain. *J. Arid. Environ.* **2011**, *75*, 377–382. [[CrossRef](#)]
27. Mitchell, J.J.; Glenn, N.F.; Sankey, T.T.; Derryberry, D.R.; Anderson, M.O.; Hruska, R.C. Small-footprint lidar estimations of sagebrush canopy characteristics. *Photogramm. Eng. Remote Sens.* **2011**, *77*, 521–530. [[CrossRef](#)]
28. Bork, E.W.; Su, J.G. Integrating LIDAR data and multispectral imagery for enhanced classification of rangeland vegetation: A meta analysis. *Remote Sens. Environ.* **2007**, *111*, 11–24. [[CrossRef](#)]
29. Li, S.; Wang, T.; Hou, Z.; Gong, Y.; Feng, L.; Ge, J. Harnessing terrestrial laser scanning to predict understory biomass in temperate mixed forests. *Ecol. Indic.* **2021**, *121*, 107011. [[CrossRef](#)]
30. Arseniou, G.; MacFarlane, D.W.; Calders, K.; Baker, M. Accuracy differences in aboveground woody biomass estimation with terrestrial laser scanning for trees in urban and rural forests and different leaf conditions. *Trees-Struct. Funct.* **2023**, *37*, 761–779. [[CrossRef](#)]
31. Arslan, A.E.; Erten, E.; Inan, M. A comparative study for obtaining effective Leaf Area Index from single Terrestrial Laser Scans by removal of wood material. *Measurement* **2021**, *178*, 109262. [[CrossRef](#)]
32. Béland, M.; Widlowski, J.-L.; Fournier, R.A.; Côté, J.-F.; Verstraete, M.M. Estimating leaf area distribution in savanna trees from terrestrial LiDAR measurements. *Agric. For. Meteorol.* **2011**, *151*, 1252–1266. [[CrossRef](#)]
33. Li, S.; Dai, L.; Wang, H.; Wang, Y.; He, Z.; Lin, S. Estimating Leaf Area Density of Individual Trees Using the Point Cloud Segmentation of Terrestrial LiDAR Data and a Voxel-Based Model. *Remote Sens.* **2017**, *9*, 1202. [[CrossRef](#)]
34. Nguyen, V.T.; Fournier, R.A.; Côté, J.F.; Pimont, F. Estimation of vertical plant area density from single return terrestrial laser scanning point clouds acquired in forest environments. *Remote Sens. Environ.* **2022**, *279*, 113115. [[CrossRef](#)]
35. Puletti, N.; Galluzzi, M.; Grotti, M.; Ferrara, C. Characterizing subcanopy structure of Mediterranean forests by terrestrial laser scanning data. *Remote Sens. Appl.-Soc. Environ.* **2021**, *24*, 100620. [[CrossRef](#)]
36. Brolly, G.; Király, G.; Lehtomäki, M.; Liang, X. Voxel-Based Automatic Tree Detection and Parameter Retrieval from Terrestrial Laser Scans for Plot-Wise Forest Inventory. *Remote Sens.* **2021**, *13*, 542. [[CrossRef](#)]
37. Zheng, G.; Moskal, L.M.; Kim, S.H. Retrieval of Effective Leaf Area Index in Heterogeneous Forests with Terrestrial Laser Scanning. *IEEE Trans. Geosci. Remote Sens.* **2013**, *51*, 777–786. [[CrossRef](#)]
38. Kükenbrink, D.; Schneider, F.D.; Leiterer, R.; Schaepman, M.E.; Morsdorf, F. Quantification of hidden canopy volume of airborne laser scanning data using a voxel traversal algorithm. *Remote Sens. Environ.* **2017**, *194*, 424–436. [[CrossRef](#)]
39. Cifuentes, R.; Van der Zande, D.; Farifteh, J.; Salas, C.; Coppin, P. Effects of voxel size and sampling setup on the estimation of forest canopy gap fraction from terrestrial laser scanning data. *Agric. For. Meteorol.* **2014**, *194*, 230–240. [[CrossRef](#)]
40. Campbell, M.J.; Dennison, P.E.; Hudak, A.T.; Parham, L.M.; Butler, B.W. Quantifying understory vegetation density using small-footprint airborne lidar. *Remote Sens. Environ.* **2018**, *215*, 330–342. [[CrossRef](#)]
41. Soma, M.; Pimont, F.; Durrieu, S.; Dupuy, J.L. Enhanced Measurements of Leaf Area Density with T-LiDAR: Evaluating and Calibrating the Effects of Vegetation Heterogeneity and Scanner Properties. *Remote Sens.* **2018**, *10*, 1580. [[CrossRef](#)]
42. Béland, M.; Baldocchi, D.D.; Widlowski, J.; Fournier, R.A.; Verstraete, M.M. On seeing the wood from the leaves and the role of voxel size in determining leaf area distribution of forests with terrestrial LiDAR. *Agric. For. Meteorol.* **2014**, *184*, 82–97. [[CrossRef](#)]
43. Soma, M.; Pimont, F.; Dupuy, J.L. Sensitivity of voxel-based estimations of leaf area density with terrestrial LiDAR to vegetation structure and sampling limitations: A simulation experiment. *Remote Sens. Environ.* **2021**, *257*, 112354. [[CrossRef](#)]
44. Menéndez-Miguélez, M.; Madrigal, G.; Sixto, H.; Oliveira, N.; Calama, R. Terrestrial Laser Scanning for Non-Destructive Estimation of Aboveground Biomass in Short-Rotation Poplar Coppices. *Remote Sens.* **2023**, *15*, 1942. [[CrossRef](#)]
45. Yao, X.; Yang, G.; Wu, B.; Jiang, L.; Wang, F. Biomass Estimation Models for Six Shrub Species in Hunshandake Sandy Land in Inner Mongolia, Northern China. *Forests* **2021**, *12*, 167. [[CrossRef](#)]
46. Besl, P.J.; McKay, H.D. A method for registration of 3-D shapes. *IEEE Trans. Pattern Anal. Mach. Intell.* **1992**, *14*, 239–256. [[CrossRef](#)]
47. Loudermilk, E.L.; Hiers, J.K.; O'Brien, J.J.; Mitchell, R.J.; Singhanaia, A.; Fernandez, J.C.; Cropper, W.P., Jr.; Slatton, K.C. Ground-based LIDAR: A novel approach to quantify fine-scale fuelbed characteristics. *Int. J. Wildland Fire* **2009**, *18*, 676–685. [[CrossRef](#)]
48. Hosoi, F.; Omasa, K. Voxel-Based 3-D Modeling of Individual Trees for Estimating Leaf Area Density Using High-Resolution Portable Scanning Lidar. *IEEE Trans. Geosci. Remote Sens.* **2006**, *44*, 3610–3618. [[CrossRef](#)]
49. Liu, X.; Wang, Y.; Kang, F.; Yue, Y.; Zheng, Y. Canopy Parameter Estimation of *Citrus grandis* var. Longanyou Based on LiDAR 3D Point Clouds. *Remote Sens.* **2021**, *13*, 1859. [[CrossRef](#)]
50. Di Gennaro, S.F.; Matese, A. Evaluation of novel precision viticulture tool for canopy biomass estimation and missing plant detection based on 2.5D and 3D approaches using RGB images acquired by UAV platform. *Plant Methods* **2020**, *16*, 91. [[CrossRef](#)]

51. Zhu, T.; Ma, X.; Guan, H.; Wu, X.; Wang, F.; Yang, C.; Jiang, Q. A calculation method of phenotypic traits based on three-dimensional reconstruction of tomato canopy. *Comput. Electron. Agric.* **2023**, *204*, 107515. [[CrossRef](#)]
52. Monsi, M.; Saeki, T. On the Factor Light in Plant Communities and its Importance for Matter Production. *Ann. Bot.* **2005**, *95*, 549–567. [[CrossRef](#)] [[PubMed](#)]
53. Yan, G.; Hu, R.; Luo, J.; Weiss, M.; Jiang, H.; Mu, X.; Xie, D.; Zhang, W. Review of indirect optical measurements of leaf area index: Recent advances, challenges, and perspectives. *Agric. For. Meteorol.* **2019**, *265*, 390–411. [[CrossRef](#)]
54. Asner, G.P.; Scurlock, J.M.O.; Hicke, J.A. Global synthesis of leaf area index observations: Implications for ecological and remote sensing studies. *Glob. Ecol. Biogeogr.* **2003**, *12*, 191–205. [[CrossRef](#)]
55. Welles, J.M.; Cohen, S. Canopy structure measurement by gap fraction analysis using commercial instrumentation. *J. Exp. Bot.* **1996**, *47*, 1335–1342. [[CrossRef](#)]
56. Hu, R.; Bournez, E.; Cheng, S.; Jiang, H.; Nerry, F.; Landes, T.; Saudreau, M.; Kastendeuch, P.; Najjar, G.; Colin, J.; et al. Estimating the leaf area of an individual tree in urban areas using terrestrial laser scanner and path length distribution model. *ISPRS-J. Photogramm. Remote Sens.* **2018**, *144*, 357–368. [[CrossRef](#)]
57. Liu, Z.; Chen, R.; Song, Y.; Han, C.; Yang, Y. Estimation of aboveground biomass for alpine shrubs in the upper reaches of the Heihe River Basin, Northwestern China. *Environ. Earth Sci.* **2015**, *73*, 5513–5521. [[CrossRef](#)]
58. Elzein, T.M.; Blarquez, O.; Gauthier, O.; Carcaillet, C. Allometric equations for biomass assessment of subalpine dwarf shrubs. *Alp. Bot.* **2011**, *121*, 129–134. [[CrossRef](#)]
59. Dahlberg, U.; Berge, T.W.; Petersson, H.; Vencatasawmy, C.P. Modelling biomass and leaf area index in a sub-arctic Scandinavian mountain area. *Scand. J. For. Res.* **2007**, *19*, 60–71. [[CrossRef](#)]
60. Kuyah, S.; Muthuri, C.; Jamnadass, R.; Mwangi, P.; Neufeldt, H.; Dietz, J. Crown area allometries for estimation of aboveground tree biomass in agricultural landscapes of western Kenya. *Agrofor. Syst.* **2012**, *86*, 267–277. [[CrossRef](#)]
61. Kalita, R.M.; Das, A.K.; Nath, A.J. Allometric equations for estimating above- and belowground biomass in Tea (*Camellia sinensis* (L.) O. Kuntze) agroforestry system of Barak Valley, Assam, northeast India. *Biomass Bioenerg.* **2015**, *83*, 42–49. [[CrossRef](#)]
62. Flade, L.; Hopkinson, C.; Chasmer, L. Allometric Equations for Shrub and Short-Stature Tree Aboveground Biomass within Boreal Ecosystems of Northwestern Canada. *Forests* **2020**, *11*, 1207. [[CrossRef](#)]
63. Zong, X.; Wang, T.; Skidmore, A.K.; Heurich, M. The impact of voxel size, forest type, and understory cover on visibility estimation in forests using terrestrial laser scanning. *GISci. Remote Sens.* **2021**, *58*, 323–339. [[CrossRef](#)]
64. Weiser, H.; Winiwarter, L.; Anders, K.; Fassnacht, F.E.; Hoefle, B. Opaque voxel-based tree models for virtual laser scanning in forestry applications. *Remote Sens. Environ.* **2021**, *265*, 112641. [[CrossRef](#)]
65. Chen, J.M.; Mo, G.; Pisek, J.; Liu, J.; Deng, F.; Ishizawa, M.; Chan, D. Effects of foliage clumping on the estimation of global terrestrial gross primary productivity. *Glob. Biogeochem. Cycle* **2012**, *26*, GB1019. [[CrossRef](#)]
66. Zou, J.; Yan, G.; Chen, L. Estimation of Canopy and Woody Components Clumping Indices at Three Mature *Picea crassifolia* Forest Stands. *IEEE J. Sel. Top. Appl. Earth Observ. Remote Sens.* **2015**, *8*, 1413–1422. [[CrossRef](#)]
67. Hu, R.; Yan, G.; Mu, X.; Luo, J. Indirect measurement of leaf area index on the basis of path length distribution. *Remote Sens. Environ.* **2014**, *155*, 239–247. [[CrossRef](#)]
68. Korhonen, L.; Vauhkonen, J.; Virolainen, A.; Hovi, A.; Korpela, I. Estimation of tree crown volume from airborne lidar data using computational geometry. *Int. J. Remote Sens.* **2013**, *34*, 7236–7248. [[CrossRef](#)]
69. Li, Q.; Gao, X.; Fei, X.; Zhang, H.; Wang, J.; Cui, Y.; Li, B. Construction of Tree Crown Three-dimensional Model Using Alpha-shape Algorithm. *Bull. Surv. Mapp.* **2018**, *12*, 91–95.
70. Olsoy, P.J.; Mitchell, J.J.; Levia, D.F.; Clark, P.E.; Glenn, N.F. Estimation of big sagebrush leaf area index with terrestrial laser scanning. *Ecol. Indic.* **2016**, *61*, 815–821. [[CrossRef](#)]
71. Martin-Ducup, O.; Robert, S.; Fournier, R.A. A method to quantify canopy changes using multi-temporal terrestrial lidar data: Tree response to surrounding gaps. *Agric. For. Meteorol.* **2017**, *237*, 184–195.
72. Latella, M.; Raimondo, T.; Belcore, E.; Salerno, L.; Camporeale, C. On the integration of LiDAR and field data for riparian biomass estimation. *J. Environ. Manag.* **2022**, *322*, 116046. [[CrossRef](#)]
73. Domingo, D.; Luis Montealegre, A.; Teresa Lamelas, M.; Garcia-Martin, A.; de la Riva, J.; Rodriguez, F.; Alonso, R. Quantifying forest residual biomass in *Pinus halepensis* Miller stands using Airborne Laser Scanning data. *GISci. Remote Sens.* **2019**, *56*, 1210–1232. [[CrossRef](#)]
74. Domingo, D.; Teresa Lamelas, M.; Luis Montealegre, A.; Garcia-Martin, A.; de la Riva, J. Estimation of Total Biomass in Aleppo Pine Forest Stands Applying Parametric and Nonparametric Methods to Low-Density Airborne Laser Scanning Data. *Forests* **2018**, *9*, 158. [[CrossRef](#)]
75. Sackov, I.; Barka, I.; Bucha, T. Mapping Aboveground Woody Biomass on Abandoned Agricultural Land Based on Airborne Laser Scanning Data. *Remote Sens.* **2021**, *12*, 4189. [[CrossRef](#)]
76. De Frenne, P.; Rodríguez-Sánchez, F.; De Schrijver, A.; Coomes, D.A.; Hermy, M.; Vangansbeke, P.; Verheyen, K. Light accelerates plant responses to warming. *Nat. Plants* **2015**, *1*, 15110. [[CrossRef](#)]
77. Verheyen, K.; Baeten, L.; De Frenne, P.; Bernhardt-Roemermann, M.; Brunet, J.; Cornelis, J.; Decocq, G.; Dierschke, H.; Eriksson, O.; Hédél, R. Driving factors behind the eutrophication signal in understorey plant communities of deciduous temperate forests. *J. Ecol.* **2012**, *100*, 352–365. [[CrossRef](#)]

78. Landuyt, D.; Maes, S.L.; Depauw, L.; Ampoorter, E.; Blondeel, H.; Perring, M.P.; Brumelis, G.; Brunet, J.; Decocq, G.; den Ouden, J.; et al. Drivers of above-ground understorey biomass and nutrient stocks in temperate deciduous forests. *J. Ecol.* **2019**, *108*, 982–997. [[CrossRef](#)]
79. Beets, P.N.; Kimberley, M.O.; Oliver, G.R.; Pearce, S.H. The Application of Stem Analysis Methods to Estimate Carbon Sequestration in Arboreal Shrubs from a Single Measurement of Field Plots. *Forests* **2014**, *5*, 919–935. [[CrossRef](#)]
80. Berner, L.T.; Jantz, P.; Tape, K.D.; Goetz, S.J. Tundra plant above-ground biomass and shrub dominance mapped across the North Slope of Alaska. *Environ. Res. Lett.* **2018**, *13*, 035002. [[CrossRef](#)]

Disclaimer/Publisher’s Note: The statements, opinions and data contained in all publications are solely those of the individual author(s) and contributor(s) and not of MDPI and/or the editor(s). MDPI and/or the editor(s) disclaim responsibility for any injury to people or property resulting from any ideas, methods, instructions or products referred to in the content.